Laser Altimeter Observations from MESSENGER's First Mercury Flyby

Maria T. Zuber, *et al.*

Science **321**, 77 (2008);
DOI: 10.1126/science.1159086

REPORT

Laser Altimeter Observations from MESSENGER's First Mercury Flyby

Maria T. Zuber,[1]* David E. Smith,[2] Sean C. Solomon,[3] Roger J. Phillips,[4] Stanton J. Peale,[5] James W. Head III,[6] Steven A. Hauck II,[7] Ralph L. McNutt Jr.,[8] Jürgen Oberst,[9] Gregory A. Neumann,[2] Frank G. Lemoine,[2] Xiaoli Sun,[2] Olivier Barnouin-Jha,[8] John K. Harmon[10]

A 3200-kilometers-long profile of Mercury by the Mercury Laser Altimeter on the MESSENGER spacecraft spans ~20% of the near-equatorial region of the planet. Topography along the profile is characterized by a 5.2-kilometer dynamic range and 930-meter root-mean-square roughness. At long wavelengths, topography slopes eastward by 0.02°, implying a variation of equatorial shape that is at least partially compensated. Sampled craters on Mercury are shallower than their counterparts on the Moon, at least in part the result of Mercury's higher gravity. Crater floors vary in roughness and slope, implying complex modification over a range of length scales.

Topography is a fundamental measurement to characterize quantitatively the surfaces of solid planetary bodies at length scales ranging from the long-wavelength shape to such local and regional processes as impact cratering, volcanism, and faulting. During the first flyby of Mercury by the MESSENGER spacecraft on 14 January 2008 (*1*), the Mercury Laser Altimeter (MLA) (*2*, *3*) successfully ranged to the planet's surface, providing the first altimetric observations of the planet from a spacecraft.

Previous measurements of the shape and topography of Mercury had been derived from Earth-based radar ranging (*4*, *5*) constrained by range observations from Mariner 10 (*6*). Because of the low inclination (7°) of Mercury's orbital plane to the ecliptic, Earth-based altimetric profiles are limited to ±12° latitude and have a spatial resolution of ~6×100 km^2 and a vertical precision of 100 m (*5*). These observations indicated a planetary reference radius of 2440 ± 1 km, an equatorial ellipticity of 540 ± 54 $\times 10^{-6}$, and an equatorial center of figure (COF) offset from the planet's center of mass (COM) of 640 ± 78 m in the direction 319.5° ± 6.9° W (*6*, *7*).

The MLA profile (Fig. 1) was acquired approximately along Mercury's equator, in a region that was in darkness during the flyby, and within the hemisphere not imaged by Mariner 10. Consequently, there are no optical images of the region in which altimetry was collected, so we used an Arecibo radar image (*8*) to correlate the profile with surface features. The MLA began ranging ~1 min before the spacecraft's closest approach and continued for ~10 min. Usable returns were received up to an altitude of 1500 km, which was larger than the expected maximum of 1200 km (*2*). As the spacecraft velocity and range from Mercury changed during the flyby, the size of laser spots on the surface varied from 23 to 134 m and the shot spacing varied from 888 to 725 m (*9*). The vertical precision varied with the received signal strength and is <15 cm at the closest range, limited by the resolution of the timing electronics. The radial accuracy of ~100 m is limited by uncertainties in the trajectory associated with errors in the ephemerides of MESSENGER and Mercury.

The profile spans ~20% of the circumference of the planet and shows a 5.2-km dynamic range of topography and 930-m root-mean-square (RMS) roughness (Fig. 1). The radius of Mercury apparently decreases by 1.4 km along the equator from ~10° to 90° E, corresponding to a 0.02° downward slope to the east. This long-wavelength surface tilt begins 30° west of the previously estimated COF/COM offset (*6*) and was not sampled in Earth-based radar altimetry (*4*). Such a long-wavelength slope, if a fundamental feature of the equatorial shape of the planet, might arise from crustal thickness or crustal density variations, global-scale mantle density variations, or topography along the planet's core-mantle boundary, which for Mercury is ~600 km beneath the surface.

The slope can be interpreted in the context of an ellipsoidal planetary shape (*10*). If we suppose that the difference in principal moments of inertia, $B - A$, is entirely a result of an ellipsoidal distribution of surface mass with density ρ_s and with semi-axes $a > b > c$, then

$$B - A = \frac{4\pi\rho_s abc}{15}\left(a^2 - b^2\right) \approx \frac{8\pi\rho_s R^4}{15}(a - b) \quad (1)$$

from which we may write

$$a - b = \frac{5}{2}R\left(\frac{B - A}{C_m}\right)\left(\frac{C_m}{C}\right)\left(\frac{C}{MR^2}\right)\frac{\langle\rho\rangle}{\rho_s} \quad (2)$$

where $A < B < C$ are the principal moments of inertia of Mercury, C_m is the moment of inertia of the mantle and crust alone, and M,

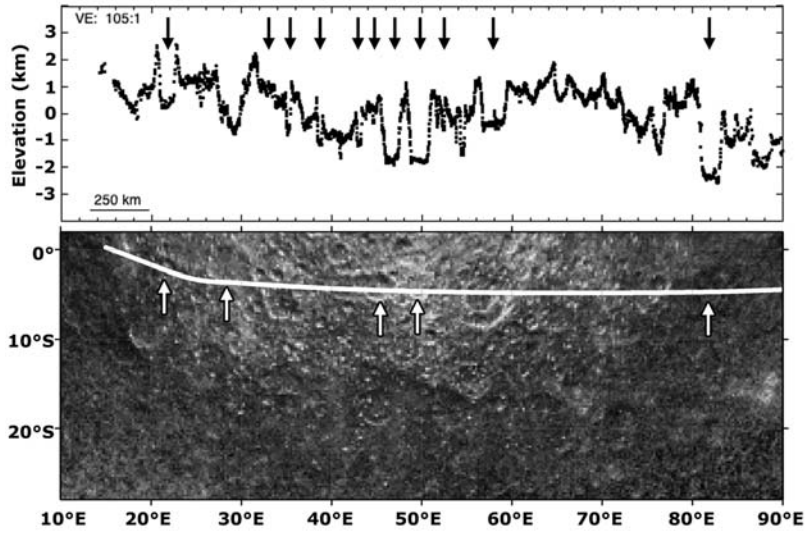

Fig. 1. (**Top**) MLA profile (vertical exaggeration 105:1). (**Bottom**) Arecibo radar image [adapted from (*8*)] with MLA profile location (white line) superposed. Arrows at top indicate locations of craters in Table 1 interpreted from detailed analysis of MLA profile points. The locations of several of the major craters are indicated by arrows on the radar image. The two-ringed circular structure in the Arecibo image at ~55 to 60°E is represented in part by a deep depression in the altimetry, but north-south radar ambiguities may be contributing to the structure in the image.

[1]Department of Earth, Atmospheric, and Planetary Sciences, Massachusetts Institute of Technology, Cambridge, MA 02139–4307, USA. [2]Solar System Exploration Division, NASA Goddard Space Flight Center, Greenbelt, MD 20771, USA. [3]Department of Terrestrial Magnetism, Carnegie Institution of Washington, Washington, DC 20015, USA. [4]Southwest Research Institute, Boulder, CO 80302, USA. [5]Department of Physics, University of California, Santa Barbara, CA 93106, USA. [6]Department of Geological Sciences, Brown University, Providence, RI 02912, USA. [7]Department of Geological Sciences, Case Western Reserve University, Cleveland, OH 44106, USA. [8]Johns Hopkins University Applied Physics Laboratory, Laurel, MD 20723, USA. [9]Institute of Planetary Research, German Aerospace Center (DLR), Berlin, D-12489 Germany. [10]National Astronomy and Ionosphere Center, Arecibo Observatory, Arecibo 00612, Puerto Rico.

*To whom correspondence should be addressed. E-mail: zuber@mit.edu

Table 1. Crater apparent slopes, RMS roughness, and pulse widths.

Longitude (°E)	Apparent floor diameter* (km)	Range (km)	Emission angle† (deg)	Apparent floor slope‡ (deg)	RMS roughness (m)	Pulse width (ns)	Spot roughness§ (m)
21.1–22.4	55.3	415	61	0.298	89.8	5.0 ± 2.1	0.3 ± 0.7
33.7–33.9	8.5	293	49	–0.451	11.8	12.4 ± 1.8	1.8 ± 3.4
35–35.3	12.8	289	48	1.26	24.3	14.6 ± 10.8	2.3 ± 2.4
38.5–38.9	17	285	44	–0.571	46.3	22.5 ± 18.4	3.8 ± 3.9
42.9–43.2	12.8	293	40	0.252	20.3	12.0 ± 10.6	1.5 ± 2.1
44.5–44.6	4.3	298	38	–0.573	7.9	19.6 ± 20.7	2.9 ± 4.0
46–47.3‖	55.4	313	36	0.177	66.5	19.3 ± 14.5	2.8 ± 2.7
48.8–50.6‖	76.7	336	34	–0.0784	31.9	20.9 ± 15.3	3.0 ± 2.7
52.3–52.4	4.3	365	31	0.117	5.7	18.0 ± 16.4	2.4 ± 2.9
56.8–59.1	98	429	26	0.0852	96.5	20.6 ± 16.7	2.7 ± 2.8
81–82.3	55.4	1020	1.5	–0.0008	110	6.3 ± 2.1	0.2 ± 0.3

*Length of MLA-crossing chord. †Emission angle is the angle between the range vector and surface normal. ‡Positive slopes are defined to be downward to the west. §Roughness from pulse width corrected for spacecraft range and emission angle. ‖Craters shown in Fig. 2.

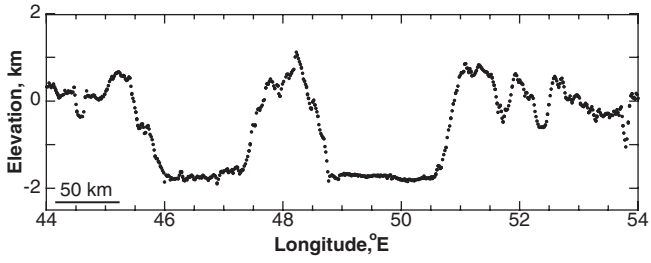

Fig. 2. Close-up of two craters showing contrast in floor roughness and tilt. The vertical exaggeration is 30:1.

R, and <ρ> are the mass, radius, and mean density of Mercury, respectively. The form of the right hand side of Eq. (2) is convenient because from measurements we have $(B - A)/C_m = (2.03 \pm 0.12) \times 10^{-4}$ (*11*), and from models we have C_m/C = 0.4 to 0.7 and C/MR^2 = 0.31 to 0.35 (*12*, *13*). The value of $(a - b)$ from MLA is 1.4 km. Surface shell densities of 2000 and 3000 kg m^{-3}, which bracket likely values, yield $(a - b)$ values of 0.26 to 0.87 km. These $(a - b)$ values are less than that observed, implying that the surface topography is at least partially compensated. The simplest explanation is that support of topography occurs by variations in crustal thickness, an inference that has also been invoked to explain Mercury's COF-COM offset by analogy with the situation on other terrestrial planets (*6*).

MLA profiled numerous depressions interpreted as impact craters on the basis of topographic expression and appearance on the Arecibo image. As on other terrestrial planets, the geomorphological complexity of impact craters on Mercury increases with diameter (*14*), with craters undergoing a transition at a diameter of about 11 km from a simple bowl shape to a planform with a flat floor, slumped walls, and a central peak (*14*). On a given planet, the ratio of depth to diameter (d/D) is uniform for unmodified complex craters, and where the MLA profile crossed close to crater centers, the ratio is ~1/40, less than on the Moon (d/D ~ 1/20). Two examples are craters in the longitude range ~45° to 50° E that have diameters (107 km and 122 km) comparable to that of Tycho (102 km), among the largest fresh craters on the Moon's nearside (Fig. 2). Whereas Tycho has a depth of 4.8 km (*15*), these craters have depths of 2.4 and 2.9 km, respectively. Although these craters may have undergone postformation modification, their substantially shallower depths in comparison to lunar counterparts is likely due at least in part to Mercury's higher surface gravity (*16*).

Crater floors may preserve evidence for modification processes that bear on geological evolution. From MLA we characterized the floors of complex craters by measuring apparent (along-track) slope, RMS roughness, and the widths of returned laser pulses, the last of which are indicative of topographic variance (due to roughness and footprint-scale slopes) within individual laser spots (*17*). Along-track slopes of 11 crater floors range from –10 m km^{-1} to +22 m km^{-1} (–0.57° to +1.26°) (*18*) (Table 1) and do not display an obvious pattern; most notably, these floor slopes do not correlate with the eastward long-wavelength slope. The RMS roughness over the approximate length scale of the crater diameter ranges from 5.7 to 110 m. Pulse widths vary considerably within individual craters, from 6 to >60 ns, indicating 2 to >20 m of vertical variability on horizontal scales of tens to hundreds of meters. For the craters studied, apparent slope, RMS roughness, and pulse widths are uncorrelated, which implies that the processes that caused tilting and created the roughness of crater floors are complex and do not operate uniformly over different length scales. Potential sources of modification include anelastic relaxation, volcanic resurfacing, tectonic subsidence, wall slumping, and ejecta emplacement from younger nearby impacts, and the variability implies that a combination of these processes operated on the profiled craters.

References and Notes

1. S. C. Solomon *et al.*, *Science* **321**, 59 (2008).
2. J. F. Cavanaugh *et al.*, *Space Sci. Rev.* **131**, 451 (2007).
3. The MLA is a time-of-flight laser rangefinder that uses direct detection and pulse-edge timing to determine precisely the range from the MESSENGER spacecraft to the target surface. MLA's laser transmitter emits 5-ns-wide pulses at an 8-Hz rate with 20 mJ of energy at a wavelength of 1064 nm. Return echoes are collected by an array of four refractive telescopes that are detected using a single silicon avalanche photodiode detector. The timing of laser pulses is measured using a set of time-to-digital converters and counters and a crystal oscillator whose frequency was monitored periodically from Earth.
4. J. K. Harmon, D. B. Campbell, D. L. Bindschadler, J. W. Head, I. I. Shapiro, *J. Geophys. Res.* **91**, 385 (1986).
5. J. K. Harmon, D. B. Campbell, in *Mercury*, F. Vilas, C. R. Chapman, M. S. Matthews, Eds. (Univ. of Ariz. Press, Tucson, AZ, 1988), pp. 101–117.
6. J. D. Anderson, R. F. Jurgens, E. L. Lau, M. A. Slade III, G. Schubert, *Icarus* **124**, 690 (1996).
7. C. F. Yoder, in *Global Earth Physics, A Handbook of Physical Constants*, T. J. Ahrens, Ed. (American Geophysical Union, Washington, DC, 1995).
8. J. K. Harmon *et al.*, *Icarus* **187**, 374 (2007).
9. The profile in Fig. 1 was computed using a reconstructed trajectory, msgr_20040803_20120401_od118.bsp, supplied by the MESSENGER navigation team.
10. In this configuration, 0° longitude coincides with one of the hot poles of Mercury, which is on the axis of minimum moment of inertia and 90° on the equator is in the direction of the intermediate axis of inertia. The radius of the ellipsoid equals a at 0° E and decreases to b at 90° E.
11. J.-L. Margot, S. J. Peale, R. F. Jurgens, M. A. Slade, I. V. Holin, *Science* **316**, 710 (2007).
12. H. Harder, G. Schubert, *Icarus* **151**, 118 (2001).
13. S. A. Hauck II, S. C. Solomon, D. A. Smith, *Geophys. Res. Lett.* **34**, L18201, 10.1029/2007GL030793 (2007).

14. R. J. Pike, in *Mercury*, F. Vilas, C. R. Chapman, M. S. Matthews, Eds. (Univ. of Arizona Press, Tucson, AZ, 1988), pp. 165–274.
15. J.-L. Margot, D. B. Campbell, R. F. Jurgens, M. A. Slade, *J. Geophys. Res.* **104**, 11875 (1999).
16. R. J. Pike, *Proc. Lunar Planet. Sci. Conf.* **11**, 2159 (1980).
17. Surface roughness and small-scale tilts, and off-nadir ranging, which occurred at angles of up to 70° during the flyby, combine to spread MLA's reflected pulse. To maximize the probability of detecting spread returns, the returned pulse is passed through three matched filters after the detector amplifier, and subsequently time-to-digital converters are employed to measure the leading- and trailing-edge times of the pulse. MLA measures pulse widths between 6 and 1000 ns, corresponding to an RMS variation in range to the surface within each laser spot of 0.4 to 64 m (*2*, *19*).
18. These apparent slopes are likely minimum values.
19. J. B. Abshire, X. Sun, R. S. Afzal, *Appl. Opt.* **39**, 2449 (2000).

20. The MESSENGER project is supported by the NASA Discovery Program under contracts NAS5-97271 to Johns Hopkins University Applied Physics Laboratory and NASW-00002 to the Carnegie Institution of Washington. We acknowledge important contributions from the MLA instrument and MESSENGER spacecraft teams.

14 April 2008; accepted 3 June 2008
10.1126/science.1159086

REPORT

Mercury Cratering Record Viewed from MESSENGER's First Flyby

Robert G. Strom,[1]* Clark R. Chapman,[2] William J. Merline,[2] Sean C. Solomon,[3] James W. Head III[4]

Morphologies and size-frequency distributions of impact craters on Mercury imaged during MESSENGER's first flyby elucidate the planet's geological history. Plains interior to the Caloris basin displaying color and albedo contrasts have comparable crater densities and therefore similar ages. Smooth plains exterior to Caloris exhibit a crater density ~40% less than on interior plains and are thus volcanic and not Caloris impact ejecta. The size distribution of smooth-plains craters matches that of lunar craters postdating the Late Heavy Bombardment, implying that the plains formed no earlier than 3.8 billion years ago (Ga). At diameters less than or equal to 8 to 10 kilometers, secondary impact craters on Mercury are more abundant than primaries; this transition diameter is much larger than that on the Moon or Mars. A low density of craters on the peak-ring basin Raditladi implies that it may be younger than 1 Ga.

Mercury has been struck by asteroids and comets since it formed, resulting not only in primary impact craters of all sizes but also in secondary craters made by reimpact of ejecta from the primary craters. Such secondaries typically have morphologies different from the pristine shapes of primary craters, and many secondary craters form clusters and chains. Geological processes such as faulting, volcanism, downslope motion, and continued cratering all degrade crater shapes, eventually erasing them by erosion or covering. The statistics of crater sizes, shapes, and spatial relations—especially their size-frequency distributions (SFDs) (*1*)—provide information (including relative ages) about the processes that formed and reshaped the cratered landscapes.

Images of Mercury by Mariner 10 from 1974 to 1975 and subsequent studies of other planetary surfaces have raised issues that the MESSENGER mission to Mercury can address (*2*), including the relative importance of secondary versus primary cratering and of volcanic versus impact-ejecta modes of plains formation. During its first flyby of Mercury, the MESSENGER spacecraft imaged portions of a crater-scarred landscape never before seen at close range. These images show the entire 1550-km-diameter Caloris impact basin (*3*) and a broad surrounding annulus of smooth plains. They also reveal diverse cratered terrains, some nearly saturated with large craters but others very sparsely cratered. Here we report preliminary analyses of crater morphology and SFD measurements from several selected regions, based chiefly on images from the narrow-angle camera (NAC) of the Mercury Dual Imaging System (*4*).

Observations of the Moon and Mars have shown that craters in the inner solar system have two SFD components (*5*, *6*). Terrains with a high density of large craters have a complex differential SFD that approximately follows a power law with a slope of –2 for crater diameter D = ~2 to 50 km. This "Population 1" was formed primarily during the Late Heavy Bombardment (LHB), characterized by large impact basins such as the Caloris basin on Mercury, only part of which was seen by Mariner 10. Younger surfaces have an SFD with a slope of –3 ("Population 2"). (Figure S1 summarizes these two SFDs.) Both impactor populations were probably derived originally from the asteroid belt (*6*). Population 1 may have resulted from size-independent ejection as gravitational resonances swept through the belt during giant-planet migration ~4 billion years ago (Ga) (*7*, *8*). Population 2 reflects impacts of near-Earth asteroids (NEAs), mainly derived by the size-dependent Yarkovsky effect that causes smaller main-belt asteroids to preferentially enter resonances and be placed into planet-crossing orbits (*9*, *10*). Heavily cratered regions of Mercury have a SFD similar to that of the highlands of the Moon and Mars (Fig. 1A). However, on Mercury and Mars, there is a dearth of craters with D < 40 km relative to the Moon (*11*). On Mercury, smaller craters were apparently removed by the formation of "intercrater plains" (*12*) during the LHB (different processes erased smaller Martian craters). The shapes of the SFDs for Mercury, Mars, and the Moon for D = 40 to 150 km (a range not affected by intercrater plains and with good statistics) match each other better if shifted somewhat in diameter, apparently because heliocentrically orbiting NEAs collide with Mercury at higher velocities and Mars at lower velocities as compared with the Moon (fig. S4).

MESSENGER data show that the northwestern half of the Caloris floor has a slightly lower albedo and different color than the southeastern half (Fig. 1C) (*3*). Could these two plains regions have been formed by volcanic episodes at widely different times? SFDs (for D > 10 km, craters unlikely to be secondaries) for these regions (Fig. 1B) (as well as for an east/west division) show no significant differences, so their ages are comparable within 10 to 20%. Until we can measure crater densities on the Caloris rims and ejecta, we cannot determine if the flooding of the floor was contemporaneous with the impact (e.g., by impact melt) or occurred later; the uncertainties nonetheless permit a lengthy period for emplacement of successive volcanic flows, particularly if they occurred after the end of the LHB when the cratering rate was low.

Since the Apollo-era discovery that the Cayley plains on the Moon were basin impact ejecta rather than of volcanic origin, a major issue in planetary geology has concerned the relative importance of volcanism in plains formation. The crater density on some of the darker exterior smooth plains that form an annulus around Caloris is about 40% lower than that on plains inside Caloris (Fig. 2A), which is consistent with

[1]Lunar and Planetary Laboratory, University of Arizona, Tucson, AZ 85721, USA. [2]Southwest Research Institute, 1050 Walnut Street, Suite 300, Boulder, CO 80302, USA. [3]Department of Terrestrial Magnetism, Carnegie Institution of Washington, 5241 Broad Branch Road, NW, Washington, DC 20015, USA. [4]Department of Geological Sciences, Brown University, Providence, RI 02912, USA.

*To whom correspondence should be addressed. E-mail: rstrom@lpl.arizona.edu